




Titan's Twilight and Sunset Solar Illumination

Jason W. Barnes^{1,3} , Shannon M. MacKenzie², Ralph D. Lorenz², and Elizabeth P. Turtle²

¹Department of Physics; University of Idaho; Moscow, ID 83844-0903, USA; jwbarnes@uidaho.edu

²Applied Physics Laboratory; Johns Hopkins University; Laurel, MD, USA

Received 2018 June 1; revised 2018 September 7; accepted 2018 September 10; published 2018 November 2

Abstract

We calculate the illumination conditions at Titan's surface using the Monte Carlo radiative transfer model `SRTC++`, motivated by the proposed Dragonfly Titan lander. We find significant surface illumination during twilight after sunset, with the twilight flux maximized near $1.0\ \mu\text{m}$ wavelength. Out to 30° past Titan's terminator, the twilight illumination exceeds that of Earth's Moon at full phase in visible red wavelengths ($0.65\ \mu\text{m}$). Imaging at night should be quite effective for stationary surface landers if they use long integration times, though it would be less effective for platforms floating on Titan's seas. Titan sunsets should be underwhelming events at visible wavelengths, with the Sun fading out while still well above the horizon and overall illumination diminishing slowly as the Sun falls below the horizon. Shadows below the lander should receive illumination from diffusely scattered light low in the sky near Titan's horizon. The total near-horizon illumination maximizes when the Sun is highest in the sky owing to the intensity of multiple scattering.

Key words: planets and satellites: individual (Titan) – radiative transfer

Supporting material: animation

1. Introduction

Titan's hazy atmosphere obscures its surface (Smith et al. 1981). Spacecraft imaging shows only the slightest hint of the surface's reflectivity when viewed at visible wavelengths ($0.6\ \mu\text{m}$ Richardson et al. 2004). Toward the red end of the visible and in the very near-infrared, surface features start to become discernible ($0.637\ \mu\text{m}$, $0.681\ \mu\text{m}$, $0.754\ \mu\text{m}$, $0.827\ \mu\text{m}$; Vixie et al. 2012). *Cassini's* Imaging Science Subsystem mapped Titan's surface at $0.938\ \mu\text{m}$ (Porco et al. 2005). To bring out the subtle variations that owe to surface reflectance, Turtle et al. (2009) combined multiple (2–5) long exposures (tens of seconds) along with division by atmospheric images at a nearby wavelength and image postprocessing.

Further out into the infrared, the atmospheric haze aerosol particles become progressively more transparent, only to be replaced with a totally different form of surface obscuration: atmospheric absorption (primarily by methane). Atmospheric gases absorb at most (75%) wavelengths of the Sun's near-infrared spectrum between 1.0 and $5.2\ \mu\text{m}$ (Barnes et al. 2007). In between absorption bands, however, the surface peeks out in a set of atmospheric windows centered on $1.08\ \mu\text{m}$, $1.3\ \mu\text{m}$, $1.6\ \mu\text{m}$, $2.0\ \mu\text{m}$, 2.7 and $2.8\ \mu\text{m}$, and $5.0\ \mu\text{m}$ (Barnes et al. 2009; Le Mouélic et al. 2012a). Those windows become progressively clearer toward longer wavelengths. While *Huygens* measured a total scattering optical depth of $\tau = 8$ at $0.55\ \mu\text{m}$ in the visible, the optical depth drops to $\tau = 2.7$ at $1.08\ \mu\text{m}$ (Tomasko et al. 2008b) and to $\tau = 0.8$ by $2.0\ \mu\text{m}$ (Barnes et al. 2013). Within the $5\ \mu\text{m}$ window, the atmosphere is nearly clear (Brown et al. 2008), with normal optical depths of only around $\tau \sim 0.05$ (Maltagliati et al. 2015a).

Many of the major outstanding questions post-*Cassini* require measurements from either on Titan's surface (from landers; Lorenz et al. 2008; Reh et al. 2009) or within the atmosphere (from balloons; Lorenz 2008; Barnes et al. 2012)). How does Titan's hazy atmosphere affect the illumination

environment in which these future in situ missions will operate? Understanding the nature of that illumination affects both the experiments that landers can perform and the design of the instruments to accomplish those experiments.

The New Frontiers Phase-A mission concept Dragonfly specifically motivates the present work (Figure 1; Turtle et al. 2018). We want to know (1) how much natural sunlight illuminates the surface early in the morning, late in the afternoon, and at night; and (2) where that light comes from to ascertain whether or not areas of interest will be in the vehicle's shadow. First, we describe our approach using a spherical Monte Carlo radiative transfer model in Section 2. We then discuss the model results in light of illumination quantity (twilight) in Section 3, and in light of illumination direction (sunset) in Section 4 before concluding in Section 5.

2. Model

Spherical Radiative Transfer in C++ (`SRTC++` Barnes et al. 2018) is a three-dimensional (3D) spherical Monte Carlo radiative transfer model developed specifically for planetary application to Titan. It uses the simple and somewhat brute-force approach of throwing millions of photons toward Titan and calculating their trajectories through the atmosphere and surface in a stochastic fashion. We track each photon in three Cartesian coordinates x , y , and z , calculating local atmospheric properties at each point along the photon's path by mapping into Titan latitude, longitude, and altitude as needed (see Barnes et al. 2018 for complete details of the `SRTC++` algorithm). `SRTC++` complements earlier plane-parallel Titan radiative transfer approaches (McKay et al. 1989; Young et al. 2002; Rannou et al. 2003; Rodriguez et al. 2006; Griffith et al. 2012; Hirtzig et al. 2013; Maltagliati et al. 2015b) by tackling problems that manifest in the spatial domain, rather than primarily spectral problems. Therefore, `SRTC++` is particularly well suited to the present task of tracking photons ping-ponging through the atmosphere onto Titan's nightside.

³ ResearcherID: B-1284-2009.

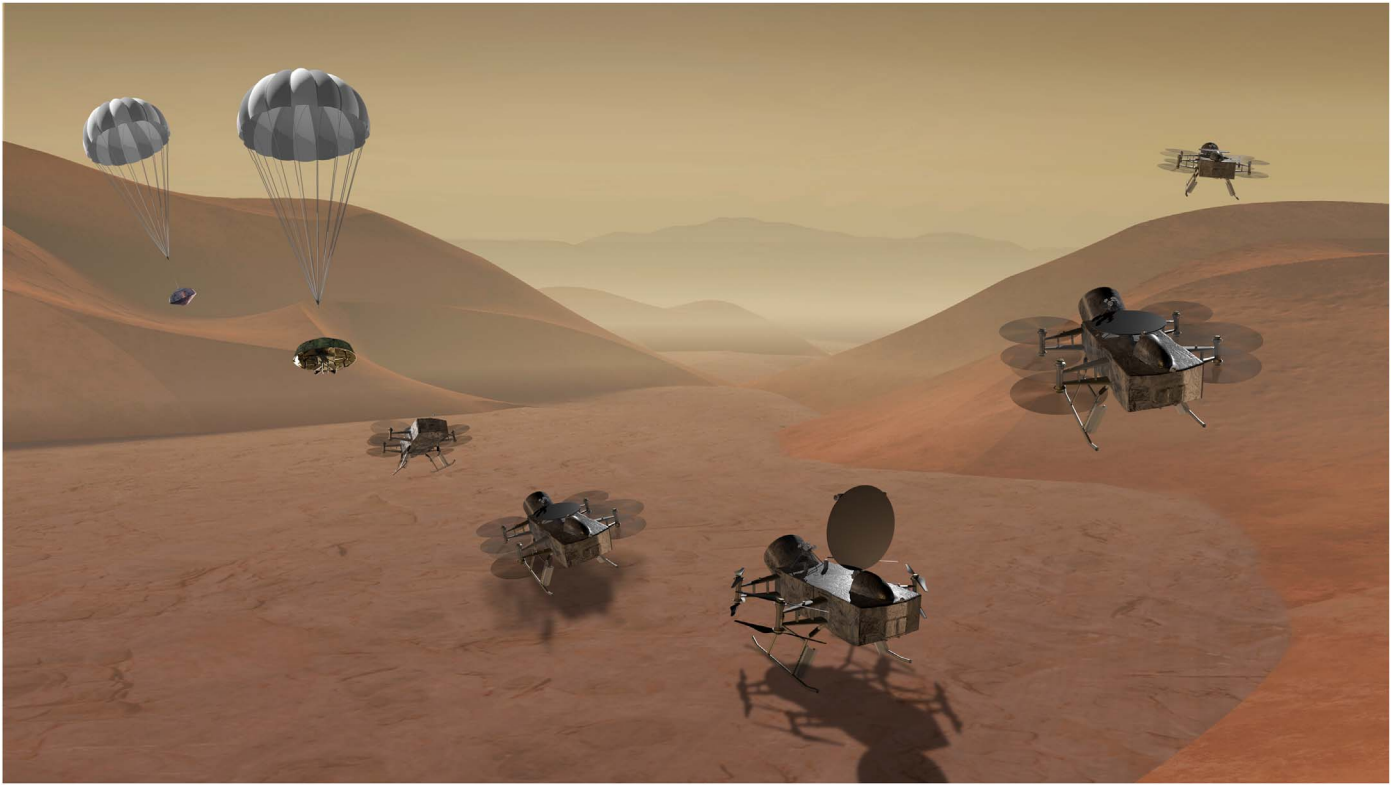


Figure 1. The Dragonfly mission concept, presently in Phase A with NASA’s New Frontiers Program, would send a relocatable rotorcraft lander to Titan’s surface to study prebiotic chemistry, assess water-based and hydrocarbon-based habitability, and search for potential chemical biosignatures. The conditions for Dragonfly’s cameras motivates the work described in this paper. See in particular the shadow depicted under the lander while in transmit mode (third Dragonfly from right)—such a sharp shadow will not occur (except maybe at $5\ \mu\text{m}$) owing to atmospheric scattering. But by how much will diffuse atmospheric illumination fill in the shadow under the lander in the sampling workspace?

2.1. Model Modifications

We approach the non-traditional nature of the radiative transfer problem by introducing a new type of detector (a program class that catches and records the result of Monte Carlo collisions) within `SRTC++` (Figure 2). The new “insolation” detector does not simulate an imaging array, but rather employs the entire Titan surface like a single gigantic detector. We split the surface into sectors with equal width in solar incidence angle arranged symmetrically around the subsolar point as shown in Figure 2. Whenever a photon hits the ground, `SRTC++` records its intensity in the appropriate solar incidence bin sector. Think of it like covering Titan in solar panels, and then recording the total power generated as a function of solar incidence angle in bins. This novel approach makes full use of each photon in the simulation and thus improves the signal-to-noise of the result by using increased detector area near the terminator where the signal is most interesting but also of low intensity.

For the case in Section 4, we generate a simulated image of the sky within each solar incidence bin. To achieve this, we record not just the total intensity at the surface but also the specific zenith distance (ZD) and azimuth angle of each photon. The ZD of the photon corresponds to its angular distance from straight up (the zenith) when it impacts the surface (as in Figure 3). While this angle might conventionally be referred to as the photon’s “incidence angle” onto the surface, we will here refer to it exclusively as ZD to differentiate it from the solar incidence angle that defines the bins, which is a fixed function of the surface latitude and longitude.

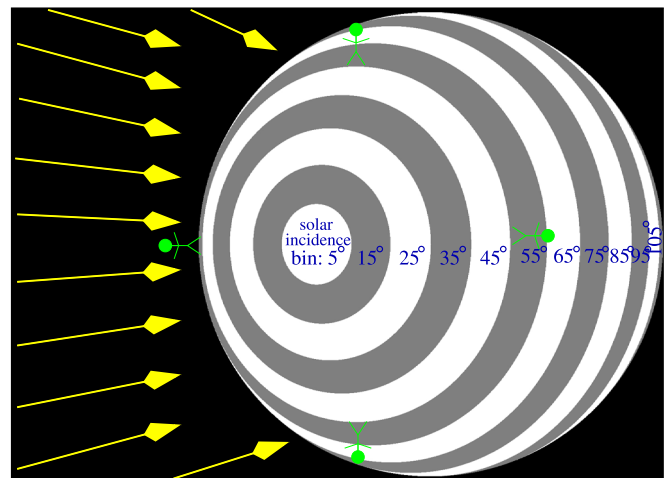


Figure 2. We develop a new detector for `SRTC++` that turns the entire surface of Titan into a sensing surface. We call this detector type “insolation.” An insolation detector breaks Titan up into a one-dimensional sequence of ring-like sectors that each constitute a bin in solar incidence angle. In the figure, we show bins that each have a width of 10° (the actual `SRTC++` run uses 2° bins). When any photon hits the surface, the detector triggers and records the intensity increment in the appropriate bin. This structure has the advantage of making productive use of each photon in the simulation to increase the signal-to-noise ratio particularly near the terminator where illumination becomes dim and the sector area is maximized. When generating sky view images, we rotate the site of each photon-surface interaction to correspond to the appropriate local sky image. Effectively, we generate the view of the little green stick-figures, each of whom sees an identical sky when looking toward the horizon in the direction of the Sun from their different vantage points around the 55° solar incidence sector.

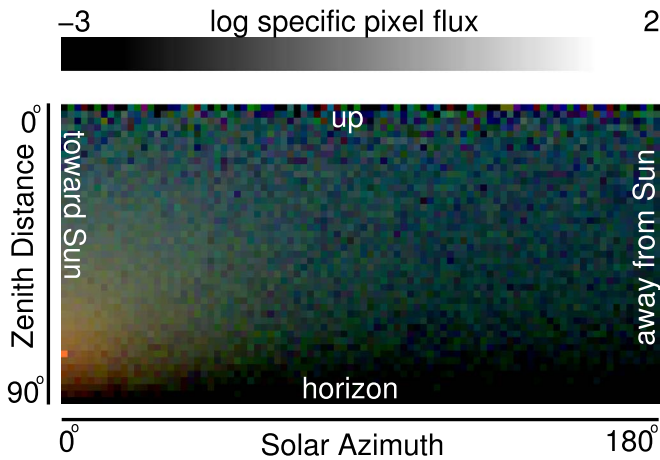


Figure 3. Here we show the style of model output for sky images, as outlined in Section 2.1. The output cube represents the sky as a cylindrical map of the hemisphere above a point on Titan for each solar incidence angle sector. The y -axis here represents zenith distance as seen by an observer at that point, with the straight up direction on Titan at the top of the image and the horizon at zenith distance of 90° at the bottom. The x -axis shows solar azimuth, with 0° being toward the Sun at left and 180° being directly away from the Sun at far right. Since the view is symmetric left-to-right, we wrap azimuths around when detecting so that negative azimuths get mapped from 0° to 180° . This particular view shows a solar incidence of 75° , and the orange pixel near lower-left is the Sun. The colors map with $0.75 \mu\text{m}$ as blue, $1.08 \mu\text{m}$ as green, and $2.0 \mu\text{m}$ as red. Direct sunlight gets quite well scattered even as far into the red as $0.75 \mu\text{m}$, hence the orange solar hue here. The image uses a logarithmic scaling between -3.0 and $+2.0$ in specific pixel flux (normalized such that a sky filled with pixels each with specific pixel flux of 1.0 will integrate to a total sky brightness of flux 1.0 as in Section 3).

To prevent the sky image from smearing out across the sector, we execute an Euler angle rotation into a common reference frame, effectively generating the image that you might see if you were standing at that spot looking toward the horizon in the direction of the Sun. The green stick-figures in Figure 2 each see the same sky view. Each sector then contains a two-dimensional array that records the sky image (Figure 3). The y -axis of the array encodes ZD with 0° (straight up) at the top and 90° (the horizon) at the bottom. That way “up” is up and “down” is down to ease interpretability. The x -axis corresponds to azimuth as an angular distance around the horizon. The Sun has 0° azimuth. It appears at the left-hand edge of a sky view. The x -axis then proceeds around to the right with increasing azimuth to 180° at the right-hand side, which corresponds to directly opposite the Sun. Because the problem is mirror symmetric left-to right, we record photons with azimuths to the left in their corresponding right-side bin.

In its present incarnation, SRTC++ does not treat refraction or polarization. For complete details of the SRTC++ model, including placing it into context with previous work, please see our model description paper Barnes et al. (2018).

2.2. Model Atmosphere

Following Barnes et al. (2018), we assume a Tomasko et al. (2008b) Titan atmosphere for our calculations for all parameters except one: single-scattering albedo. We add visible-wavelength single-scattering albedos for wavelengths less than $0.9 \mu\text{m}$ and use modified values for infrared wavelengths longer than $0.9 \mu\text{m}$. We describe the atmosphere and the single-scattering albedo modifications below.

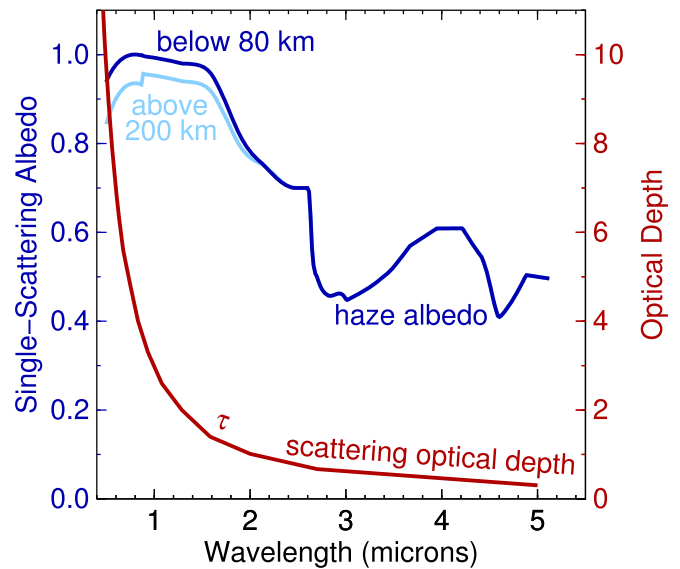


Figure 4. The parameters of Titan’s atmosphere as we model it. We show the haze scattering optical depths in red, with scale on the right, and we plot the haze single-scattering albedos in blue, with scale on the left. The optical depths come from Tomasko et al. (2008b); they represent *Huygens* measurements shortward of $1.6 \mu\text{m}$ but the values toward $5 \mu\text{m}$ come from extrapolation based on a haze aerosol particle model. The atmospheric single-scattering albedos come from two different data sets: Hirtzig et al. (2013) in the infrared, and Doose et al. (2016) in the visible. Hence the seam at $0.9 \mu\text{m}$, the switchover point. We linearly interpolate the two albedos in between 80 km and 200 km.

We show the one-way haze scattering normal optical depth of the entire Titan atmosphere in the Tomasko et al. (2008b) model in Figure 4 (in red, right-hand scale). The optical depths from $0.4 \mu\text{m}$ out to $1.6 \mu\text{m}$, where the *Huygens* Descent Imager Spectral Radiometer (DISR) detector cut off, are quite accurate. The optical depths extrapolated beyond there become increasingly uncertain, such that the DISR optical depth $\tau = 0.3$ at $5.0 \mu\text{m}$ greatly exceeds numbers obtained from occultations ($\tau \sim 0.05$; Maltagliati et al. 2015a). Therefore our results for $5 \mu\text{m}$ should be considered as upper limits based on this too-opaque atmospheric assumption. We continue to work on refining higher-fidelity models, however, and we hope to be able to incorporate improvements into the atmospheric model in the future.

The haze phase functions derive from DISR measurements from within the atmosphere. We use the two different haze phase functions as specified by Tomasko et al. (2008b): one below 80 km altitude, and the other above 80 km altitude.

We assume no gaseous absorption within the atmosphere as SRTC++ does not yet treat gas independent from haze. So the model only generates accurate results within Titan’s atmospheric windows. Total gaseous absorption within the windows is near zero or effectively zero (Tomasko et al. 2008a), although absorption lines at some wavelengths not within windows can become appreciable even within the visible-wavelength range. Karkoschka & Tomasko (2010) shows methane absorption coefficients of 0.000 at $0.526 \mu\text{m}$, for example, 0.001 $(\text{km-am})^{-1}$ at $0.556 \mu\text{m}$, 0.011 $(\text{km-am})^{-1}$ at $0.634 \mu\text{m}$, 0.024 $(\text{km-am})^{-1}$ at $0.750 \mu\text{m}$, 0.011 $(\text{km-am})^{-1}$ at $0.828 \mu\text{m}$, and 0.028 $(\text{km-am})^{-1}$ at $0.938 \mu\text{m}$. Lemmon et al. (2002) derived a total methane column atmospheric abundance of 2.63 ± 0.17 km-am from *Hubble Space Telescope* measurements. Therefore, depending on the local methane humidity, our neglecting of gaseous methane absorption can overestimate

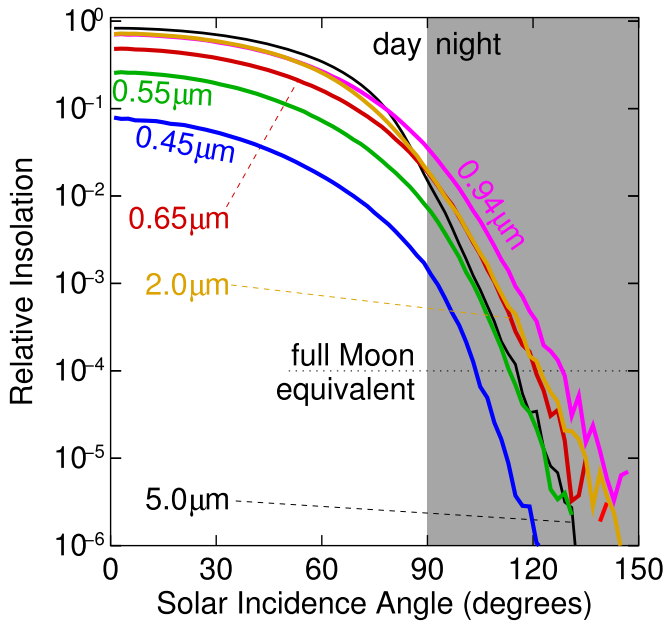


Figure 5. We plot here the solar illumination that makes it down to the surface, relative to that you would measure at the subsolar point on an atmosphereless planet, as a function of angular distance from that subsolar point in degrees (the solar incidence angle). Given that Titan’s exospheric insolation corresponds to roughly 1% that on Earth, and that the full Moon’s illumination at Earth is about a million times less intense than that of the Sun, we place a line to indicate where the illumination might roughly correspond to that of Earth’s Moon when full. The terminator is at 90°. Beyond 90°, solar incidence represents the twilight illumination of Titan’s nightside. Although the twilight illumination peaks at around 1 micron wavelength, both 2 micron and 0.65 micron bands prove nearly as good. For each of these, we calculate that illumination at the surface should be enough to image out to at least 30° beyond the terminator, although long exposure times would be helpful.

illumination by potentially up to a few tens of percent within these visible and near-infrared windows.

We also do not treat Rayleigh scattering as it has not yet been incorporated into SRTC++. Rayleigh scattering can be significant at optical wavelengths with appreciable optical depths (>0.2) below $0.8 \mu\text{m}$ (Young et al. 2002). It is not immediately evident whether incorporation of Rayleigh scattering would increase or decrease twilight illumination; however, we leave incorporation of Rayleigh effects to future work.

For the haze single-scattering albedo, we assume values from Doose et al. (2016) for wavelengths shorter than $0.9 \mu\text{m}$. As recommended by Doose et al. (2016), we have one single-scattering albedo for below 80 km, another one for above 200 km, and we interpolate linearly in between. Beyond $0.9 \mu\text{m}$, the single-scattering albedos are modified after Hirtzig et al. (2013) to fit observed spectra.

3. Twilight

To understand potential illumination at the Dragonfly landing site, we use SRTC++ to determine the flux of sunlight at the surface as a function of solar incidence angle. We normalize to the flux at the subsolar point of an atmosphereless planet; hence that case would yield a flux of 1.00. We present the result in Figure 5.

3.1. Wavelength Dependence

As expected, the flux maximizes at 0° solar incidence and drops broadly as the cosine of solar incidence toward 90° .

However, because SRTC++ models scatter three-dimensionally around a spherical Titan, Figure 5 continues past the terminator and beyond 90° solar incidence. The results show significant lingering twilight illumination up to 30° beyond the terminator (around 32 hr past sunset if near Titan’s equator) for $0.65 \mu\text{m}$ in the visible and also for 0.94 and $2.0 \mu\text{m}$ into the infrared.

Understanding the differing twilight behavior with wavelength requires reference back to our atmospheric parameters from Figure 4.

Starting with the simplest case first, in the $5.0 \mu\text{m}$ band, the overall optical depth is low ($\tau = 0.3$) and so is the haze single-scattering albedo (0.5). This far into the infrared, a decent fraction of sunlight makes it down to the surface undisturbed. Therefore, the $5.0 \mu\text{m}$ curve (black in Figure 5) most closely resembles a pure cosine. It starts higher than other wavelengths at 0° solar incidence. But then the illumination quickly plummets near the terminator (90° solar incidence) and dives downward after sunset. Yet, even with such a thin atmosphere and dark haze, illumination remains above 10^{-4} until 30° past the terminator. However, this result likely represents an overestimate of twilight illumination at $5 \mu\text{m}$ owing to the Tomasko et al. (2008b) overestimation of optical depth in the $5 \mu\text{m}$ window.

In the $2 \mu\text{m}$ window, the optical depth has increased to a still-modest $\tau = 0.8$. The atmospheric single-scattering albedo is higher here (around 0.8 as well), but still lower than it is at wavelengths shorter than $2 \mu\text{m}$. We draw the $2 \mu\text{m}$ flux in yellow in Figure 5. The direct solar contribution at low solar incidence remains high because a significant fraction of photons still arrive at the surface unscathed. But now the illumination improves relative to that at $5 \mu\text{m}$ approaching the terminator, where $2 \mu\text{m}$ finally becomes higher than that at $5 \mu\text{m}$. The high slant optical depth (Fortney 2005) through the atmosphere at the terminator still provides enough scattering to light the surface at a flux of 10^{-6} out to over 50° past the terminator.

The Cassini window at $0.94 \mu\text{m}$ ends up providing the highest nighttime illumination (magenta in Figure 5). At $0.94 \mu\text{m}$, the haze is super bright—near an albedo of 1.00—and the optical depth has increased to $\tau = 3.3$. The thick atmosphere combined with little or no absorption when photons scatter off of the bright haze particles leads to a huge amount of light bouncing around in the atmosphere. So much light arrives at the surface that the surface flux remains above 10^{-6} a full 60° beyond nightfall. Our result that $0.94 \mu\text{m}$ slight should reach well beyond Titan’s terminator is broadly consistent with imaging from Cassini’s camera in which surface features can easily be detected beyond the terminator (e.g., Turtle et al. 2011).

The parameters that work to the advantage of $0.94 \mu\text{m}$ light become progressively less helpful toward shorter and visible wavelengths. At $0.65 \mu\text{m}$ (roughly corresponding to the color red as visible to the human eye), the optical depth has nearly doubled to $\tau = 6$. That increased optical depth improved illumination at $0.94 \mu\text{m}$. But here at $0.65 \mu\text{m}$, the higher optical depth starts to work against high illumination because the atmospheric single-scattering albedo has dropped down from its peak. The single scattering remains above 0.95, but with the increased optical depth the number of scatters that each photon packet experiences on the way down means that more light gets absorbed within the atmosphere. Still, twilight illumination at $0.65 \mu\text{m}$ remains quite good, with a flux above 10^{-4} out 30° beyond the terminator—only a factor of three or so below the

Table 1
Comparing SRTC++ to *Huygens* ULVS

| Seq | Cycle | Time (s) | Altitude (km) | Azimuth (°) | Spectral Radiance $\left(\frac{W}{m^2 \mu m sr}\right)$ | | | |
|-----|-------|-------------|------------------|----------------|---|--------------|--------------|--------------|
| | | | | | 0.94 μm | 0.65 μm | 0.55 μm | 0.48 μm |
| 719 | 63 | 8225.41 | 3.052 | 187.89 | 0.6791 | 1.3493 | 0.9717 | 0.4467 |
| 721 | 64 | 8234.58 | 3.007 | 124.90 | 0.8558 | 1.4865 | 1.0052 | 0.4451 |
| 727 | 67 | 8323.32 | 2.576 | 287.58 | 1.5952 | 1.7587 | 1.0695 | 0.4447 |
| 731 | 69 | 8371.80 | 2.342 | 308.63 | 2.2209 | 1.9317 | 1.1098 | 0.4531 |
| 747 | 77 | 8568.21 | 1.405 | 83.75 | 1.9044 | 1.7766 | 1.0578 | 0.4407 |
| 763 | 85 | 8765.24 | 0.481 | 225.19 | 0.7 | 1.3058 | 0.9168 | 0.4080 |
| ... | ... | average | ... | average | 1.326 | 1.601 | 1.022 | 0.440 |
| ... | ... | SRTC++ | 0 | (all) | 1.00 | 1.22 | 0.76 | 0.22 |

Note. *Huygens* probe Upward-Looking Visual Spectrometer (ULVS) measurements of sky brightness as compared to sky-average brightnesses generated by our radiative transfer model SRTC++.

relative flux at the 0.94 μm optimum and about equivalent to that at 2.0 μm . With the Sun's increased brightness at 0.65 μm relative to its output at 0.94 μm , the 0.65- μm red band makes an excellent choice for bright nighttime illumination.

At shorter wavelengths, the situation degrades. By 0.55 μm (visible green) the optical depth has increased to $\tau = 8$, and the haze's single-scattering albedo has dropped further. That combination yields lower overall illumination at 0.55 μm (green) than at 0.65 μm (red) by a factor of two at every solar incidence angle.

By 0.45 μm (visible blue), the situation becomes dire for twilight imaging. An optical depth of $\tau = 12$ combined with single-scattering albedos hovering around 0.9 drive particularly low illumination at 0.45 μm as compared to anywhere else within the atmospheric windows. Even at the subsolar point, the 0.45 μm , blue light flux is less than one tenth.

Scattering of Saturnshine should operate similarly to that of sunlight (replace the x -axis of Figure 5 with angular distance to the sub-Saturn point instead and scale all of the the values appropriately for the intensity of Saturnshine—a factor of ~ 1500 for full phase with Saturn's approximate visible-wavelength albedo). Adding such a Saturnshine result to that from the actual Sun yields the result that illumination on the Saturn-facing hemisphere of Titan, and particularly at the sub-Saturn point itself, may never drop below full Moon equivalent at any time of day.

The effect of surface albedo on twilight illumination turns out to be small; see the Appendix for a detailed discussion.

We compare our sky-average brightness calculations to the measurements made by the *Huygens* Upward-Looking Visual Spectrometer⁴ (ULVS) in Table 1. The SRTC++ results consistently show lower sky-average fluxes than the measurements made by ULVS. The ULVS field of view preferentially points closer to zenith, however, and thus should measure a higher directional flux than SRTC++ calculates including the darker near-horizon sky, as we show in the next section. Alternately, the discrepancy may result from our neglect of Rayleigh scattering, which should be preferentially more important toward shorter wavelengths.

4. Sunset

While the previous section discusses the total, sky-integrated surface flux, here we turn to the distribution of incoming

sunlight as a function of position within the sky. Coincident with the SRTC++ run for Figures 5, we track the direction from which those incident photons arrive at the surface. With $2^\circ \times 2^\circ$ binning, the resulting sky images have 90 pixels across and 45 pixels vertically as displayed in in the animation of Figure 6.

Grieger (2005) executed a similar analysis of Titan's lighting conditions. Our work contains several improvements on that previous study. (Grieger 2005) used a plane-parallel approximation (Grieger et al. 2003), while we employ a fully spherical 3D calculation. In addition, Grieger (2005) did not have the benefit of *Huygens* results available to use as inputs, while we make extensive use of DISR optical depths, single-scattering albedos, and haze phase functions (Tomasko et al. 2005, 2008a, 2008b; Doose et al. 2016).

4.1. Sunset Movies

The sunset movie at 5 μm (Animated Figure 6a), showing progression in solar incidence angle from 1° (Sun almost directly up) to 99° (Sun 9° below the horizon), proves the most familiar (at right in static version). With an atmospheric one-way normal optical depth of $\tau = 0.3$, at 5 μm most of the solar flux arrives directly from the Sun without having been scattered in the atmosphere. Hence, the white dot at the left-hand side of the animation represents the Sun. But some light does come from all around the atmosphere, with a particular concentration within 20° of the Sun: the solar aureole, which results from the highly forward-scattering nature of Titan's hazes.

Even with this overestimated $\tau = 0.3$ atmosphere, the solar disk can be seen all the way down to the horizon. If you were on Titan and had 5 μm vision, you could see the Sun disappear below your local horizon. As the Sun nears sunset, the animation shows a fan-like structure in forward-scattered light emerging above the Sun itself, akin to those seen in Martian sunsets (example shown in Figure 7).

The second sunset movie (animated Figure 6(b); center of static version) shows a color version of the increasing solar incidence angle sequence with red as 2.0 μm , green as 1.08 μm , and blue as 0.75 μm , as in Figure 3. As such, these colors show a range of atmospheric scattering optical depth from $\tau = 0.8$ through $\tau = 4.8$. The solar disk is visible at each of these wavelengths when the Sun is overhead. But as the Sun approaches the horizon, the Sun reddens owing to increased slant optical depth. While the actual sunset would be visible at

⁴ Data acquired from Planetary Data System Atmospheres node, data set ID HP-SSA-DISR-2/3-EDR/RDR-V1.0.

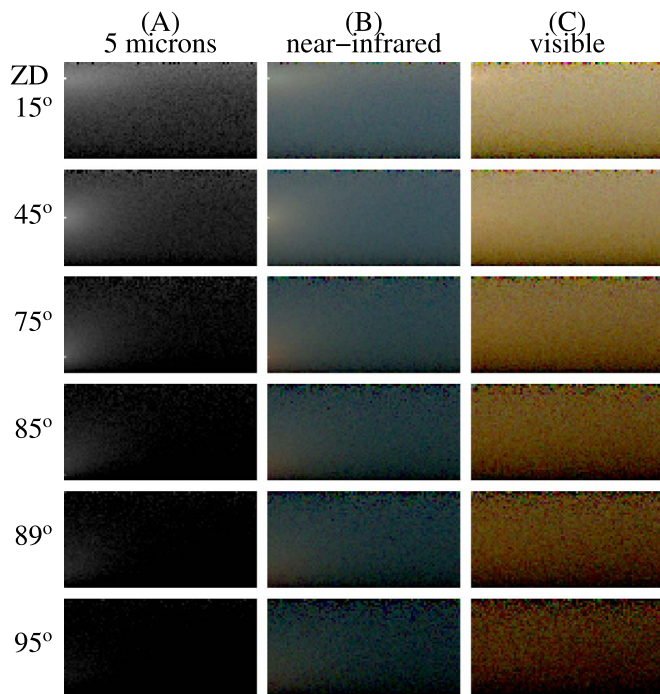


Figure 6. This set of three figure columns shows a sequence of time steps arranged into movies of the sky at $5\ \mu\text{m}$ (A), at a suite of three near-infrared wavelengths (B), and at visible wavelengths (C). Each view is scaled logarithmically to simultaneously bring out the brightness of the solar disk and relatively lower illumination from around the sky. In (A) and at $2\ \mu\text{m}$, the Sun remains visible all the way down to the horizon. In the near-infrared view in B (red = $2\ \mu\text{m}$, green = $1.08\ \mu\text{m}$, blue = $0.75\ \mu\text{m}$), the Sun remains visible until just above the horizon, when it fades away before hitting the horizon at the shorter wavelengths. The overall sky in B shows a hint of blue owing to the higher optical depth and broader scattering phase function at shorter wavelengths. In the visible-light view shown in C (red = $0.65\ \mu\text{m}$, green = $0.55\ \mu\text{m}$, blue = $0.45\ \mu\text{m}$), haze renders the sky a featureless orange with just a weak spot of the solar disk appearing when the Sun is near zenith. An animation of these figures is available. The video shows the $5\ \mu\text{m}$, (top), near-infrared (middle) and visible (bottom) wavelengths starting at ZD = 0 and ending at ZD = 95. The video duration is 26 s. (An animation of this figure is available.)



Figure 7. NASA public image release PIA07997 (credit: NASA/JPL-Caltech/Texas A&M/Cornell), showing a Martian sunset as viewed from Mars Exploration Rover *Spirit* on 2005 May 19.

$2\ \mu\text{m}$, at shorter wavelengths the Sun would fade out before encountering the horizon, similar to the experience of a sunset in the dusty Arabian desert on Earth.

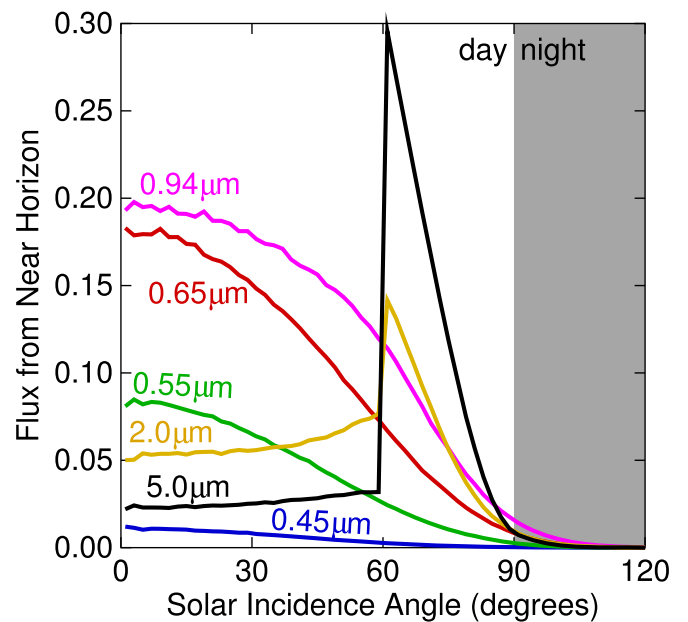


Figure 8. The above graph depicts the total flux expressed as (n.b. *not* the fractional flux) illuminating the surface from within 30° of the horizon in the sky as I_{horizon}/I_0 where I_0 is the incident exoatmospheric flux. Direct solar flux dominates at longer wavelengths where the atmosphere is most transparent ($5.0\ \mu\text{m}$, $2.0\ \mu\text{m}$). At wavelengths of $1\ \mu\text{m}$ and shorter, haze scattering dominates the surface signal, and hence the near-horizon illumination displays a maximum with the Sun highest in the sky.

Animated Figure 6(c) shows the sunset progression as it would appear in visible light. Near zenith, the solar disk would be visible, though much decreased in intensity akin to viewing the Sun through thick smoke on Earth.⁵ As the Sun drops to around 30° above the horizon the disk fades out, leaving just scattered light coming nearly uniformly from around the upward hemisphere. At visible wavelengths, the sky appears as nearly featureless orange soup most of the time, with little if any increased brightness toward the Sun's azimuth. Interestingly, even though these views assume a white surface, the Titan sky becomes darker near the horizon at all times of day, the opposite of that seen on Earth with its lower optical depth and Rayleigh scattering.

4.2. Diffuse Near-horizon Illumination

Part of the motivation for the present work is to understand the illumination environment under the Dragonfly lander when it is on the surface of Titan. To answer this question, we integrate the total amount of surface illumination arriving at the surface from within 30° of the horizon as a representation of light filling in the lander's shadow. We plot the result in Figure 8.

At $5\ \mu\text{m}$, where most of the surface illumination arrives directly from the Sun unscattered by the atmosphere, the overall flux coming from within 30° of the horizon is low until the Sun itself comes within this band when the near-horizon flux shows a huge step increase. The effect at $2\ \mu\text{m}$ resembles that at $5\ \mu\text{m}$, only with stronger scattering and a smaller step-function increase as the solar disk drops.

⁵ JWB and SMM were able to stare directly at the Sun and view sunspots though thick smoke blanketing the Pacific northwest during fires in 2015 August and 2017 September. The eerie effect was just like looking through a telescope with a solar neutral-density filter.

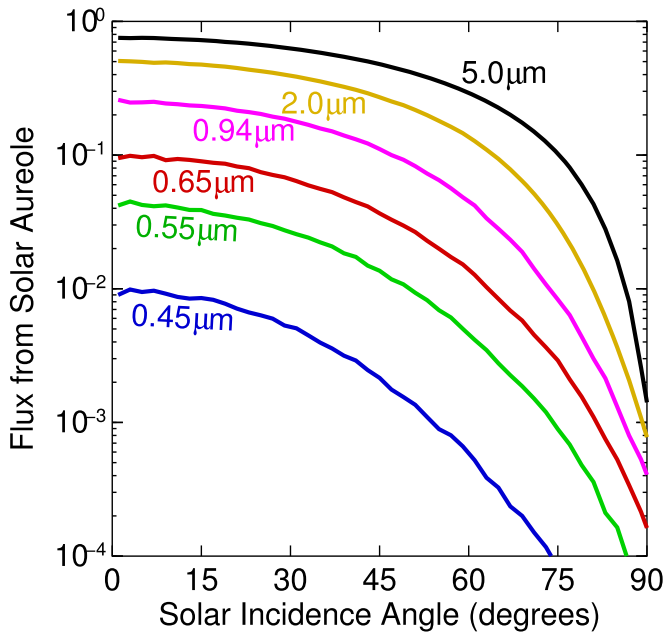


Figure 9. Direct solar flux plus that from the solar aureole, within 15° of the Sun’s disk, as I_{aureole}/I_0 . The progression is smooth since atmospheric optical depth increases as functions of both wavelength and solar incidence. The difference between this plot and the one in Figure 5 is that Figure 5 plots all-sky illumination while here we only include the direct beam and solar aureole.

Down at 0.94 , 0.65 , 0.55 , and $0.45 \mu\text{m}$, scattering dominates the near-horizon illumination. Therefore, the amount of light filling in shadows at visible wavelengths will be maximized not when the Sun itself is near the horizon, but rather when strong sunlight permeates the atmosphere when the Sun is near zenith. Like an overcast day on Earth, the near-horizon illumination shows no vestige of the actual location of the Sun in the sky, but rather results from the total amount of sunlight entering the system.

4.3. Solar Aureole

As viewed extensively by *Huygens* (Tomasko et al. 2005), the solar aureole is a halo of enhanced brightness surrounding the Sun seen from within Titan’s atmosphere. Intense forward-scattering of solar photons off of haze generates the aureole. To complement the generally scattered component shown in Figure 8, we show the total integrated flux arriving at the surface from within 15° of the Sun’s location in Figure 9.

As expected, the total surface flux coming from near the Sun maximizes at $5 \mu\text{m}$ where the haze scatters least, and the near-Sun flux minimizes at $0.45 \mu\text{m}$ where the atmosphere scatters most.

Note that the curves we plot in Figure 9 also include the direct solar component coming from within 0.05° of the position of the Sun. We show our extracted solar aureole profile of the average sky brightness as a function of distance from the Sun’s position in Figure 10, which allows for easier separation of the two components.

Figure 10 shows that the sky brightness of the aureole, without the direct portion, maximizes near $1 \mu\text{m}$. As is the case with twilight illumination (Section 3), the “just right” combination of high-but-not-too-high optical depth with high atmospheric single-scattering albedo at $0.94 \mu\text{m}$ generates the highest aureole intensity. At $5 \mu\text{m}$, the thin atmosphere lets most sunlight straight through and scatters little additional light into the aureole. At $0.55 \mu\text{m}$, the high atmospheric opacity scatters light every which way in the atmosphere and not

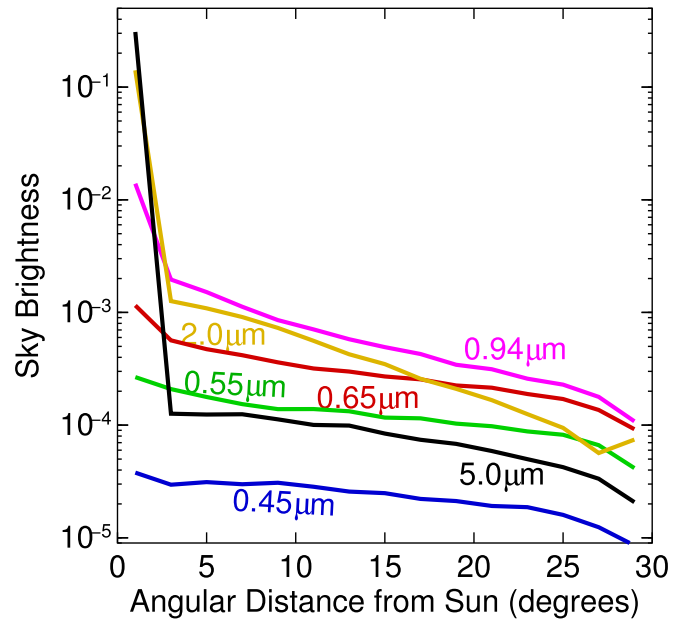


Figure 10. These profiles of average sky intensity ($\frac{I}{\Omega}$ per steradian) as a function of distance from the solar disk (assumed to be at 45° zenith distance) allow separation of the direct solar component (below 3°) and the solar aureole, composed of highly forward-scattered light.

preferentially in the aureole. But the aureole’s semi-direct solar component is most intense near $1 \mu\text{m}$, though the maximum is sufficiently broad that the aureole at $2 \mu\text{m}$ and that at $0.65 \mu\text{m}$ both strongly resemble the one at $0.94 \mu\text{m}$.

5. Conclusion

We calculate the illumination conditions at Titan’s surface as a function of both solar incidence angle (between 0° and 180°) and wavelength (0.45 , 0.55 , 0.65 , 0.94 , 2.0 , and $5.0 \mu\text{m}$). We use the radiative transfer model *SRTC++* for this task because *SRTC++* is fully spherical and accounts for the multiple scattering component critical for understanding illumination near Titan’s terminator.

We find considerable twilight illumination—the total surface brightness diminishes only to 0.01% of that at noontime 30° past Titan’s terminator at $0.65 \mu\text{m}$ (the wavelength of visible red light). Stationary landed missions on Titan’s solid surface, like the Dragonfly rotorcraft, should therefore have no trouble imaging between 0° and 30° beyond Titan’s terminator (corresponding to between local 6:00PM and local 8:00PM or from local 4:00AM to 6:00AM for landed missions near Titan’s equator). Such imaging would require longer exposure times than at local noon but might acquire decent images nonetheless; the details of exposure time and signal-to-noise ratio depend on the specifics of each camera’s optical system. Note that while Titan viewed at high phase angle appears brighter than Titan viewed at low phase angle as viewed from outside the atmosphere (García Muñoz et al. 2017), at Titan’s surface, the illumination at decreases consistently as distance from the subsolar point increases.

The situation might not be as rosy for nighttime imaging from a moving, floating platform like the previously proposed *Titan Mare Explorer (TiME)* mission (Lorenz et al. 2012). If *TiME* were to fly on the same interplanetary trajectory as Dragonfly, which has a launch date in 2025 and arrives at Titan in 2034, then it would arrive in northern winter. The entire arctic lake district would be

enshrouded in polar night (Lorenz & Newman 2015). The diffuse twilight illumination from sunlight scattered beyond the terminator would be the only natural light such a lander would ever receive. Further occlusion or reflection of light from nighttime winter polar clouds (Griffith et al. 2006; Le Mouélic et al. 2012b; Anderson et al. 2014) would complicate the problem further. Therefore, a capsule floating on one of Titan’s Maria during the winter might either require camera stabilization for long integration times or would need to bring its own light source.

Sunsets on Titan would not be very spectacular at visible wavelengths. Owing to the high optical depth of haze scattering in the visible, the sky should remain a nearly uniform orange once the Sun dips within about 30° of the horizon, and will gently fade out as the Sun physically sets. More familiar and impressive sunsets would remain accessible within Titan’s near-infrared spectral windows.

Dragonfly’s sampling workspace is below the lander, and potentially subject to shadowing by the rotorcraft fuselage. However, we show that the atmospheric scattering at visible wavelengths diffusely illuminates the surface such that even shadowed areas receive greatest total solar flux near local noon. At longer wavelengths out into the near-infrared, direct illumination takes over and oblique solar illumination might improve observations beneath the lander. Potentially complex reflections off of Titan’s surface, as might occur with broad specular reflections off of wetted terrain (Dhingra et al. 2018), would also affect lighting conditions.

Because we have assumed only Tomasko et al. (2008b) *Huygens* atmospheric parameters, our calculations do not fully describe actual Titan conditions in all cases. *Huygens* landed at $10^\circ 6'S$ $192^\circ 3'W$ during mid-summer in the Southern hemisphere (L_s 290°). Except for clouds (e.g., Roe et al. 2005), Titan’s atmospheric structure does not vary strongly around longitudes at a particular fixed latitude. Haze and methane do vary significantly in different latitude zones. Radiative transfer fitting of spectra (Hirtzig et al. 2013) match between $40^\circ S$ and $40^\circ N$ latitude using the *Huygens* haze profile increased or decreased by $\pm 20\%$. Near-infrared stellar occultations from *Cassini*/VIMS show strong differences in haze poleward of $\sim 55^\circ$ latitude (Sotin et al. 2016). Occultations only reach down to altitudes as low as Titan’s tropopause—specular reflections yield optical depths down to the surface but at only a single point so far (Barnes et al. 2013). Those occultations that we do have also indicate changes as a function of time (Maltagliati et al. 2015a), presumably owing to seasonal variation. In no case does a complete and reliable Titan atmospheric profile exist anywhere other than that obtained by *Huygens*. Therefore, our work using that *Huygens* profile represents a reasonable first step in lieu of comprehensive knowledge of atmospheric variability on Titan.

Future exploration missions will attempt to answer the considerable scientific questions outstanding after *Cassini*. Beyond the specifics of Dragonfly, other studies of post-*Cassini* missions (Levine et al. 2005; Lunine et al. 2005; Lorenz et al. 2008; Reh et al. 2009; Sittler et al. 2006; Reh et al. 2007; Coustenis et al. 2009) and floating sea capsules (Stofan et al. 2010, *TiME*;) depend on Titan’s surface illumination conditions for planning future observation approaches. In particular, visibility of Saturn in the night sky would provide a navigational aid for aerial platforms (Lorenz 2002). Future Titan orbiter missions (Sotin et al. 2017) may make use of the prospect for observing surface contrasts beyond the terminator with near-IR imaging, a problem that we will address in a future paper.

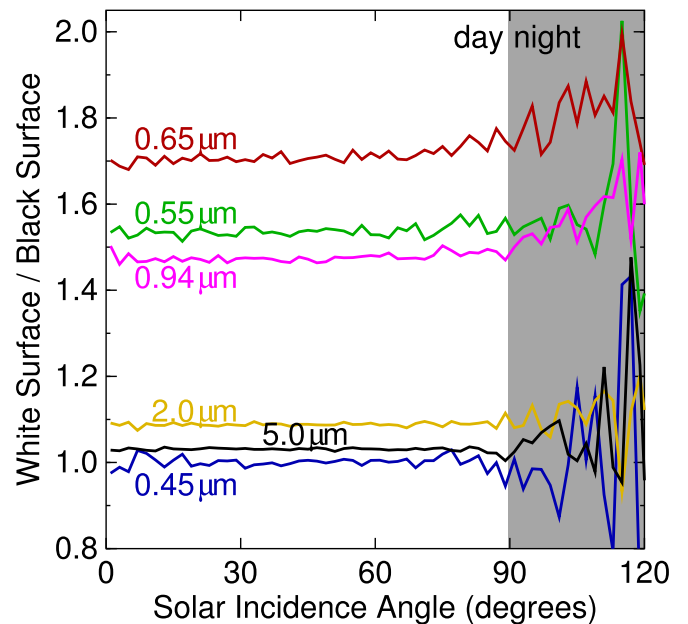


Figure 11. The difference between using a black (i.e., fully absorbing) Titan surface, as for Figure 5, and a white one. The ratio does not change with solar incidence angle except slightly beyond the terminator. But in any case, the difference remains less than a factor of two. This SRTC++ simulation used 17 million photons, which took around 3–20 hr depending on the wavelength. The wiggling lines derive from random errors that become more prominent in the ratio.

Appendix Surface Albedo Dependence

The calculations in Section 3 assume a pitch-black Titan surface with albedo equal to 0.0. Hence, Figure 5 represents the worse-case of atmosphere-only illumination. We show the effect of transforming the surface into a white, fully reflective surface with an albedo of 1.0 in Figure 11.

Unsurprisingly, the white surface increases illumination overall as light can reflect off the ground and then off the haze again and back down to the ground. At 5.0 and 2.0 μm , where the haze is thin, dark, and forward-scattering, the white surface has less than a 10% effect. Similarly, at 0.45 μm where the atmosphere has both high optical depth and a somewhat low single-scattering albedo, so much light is lost by the time sunlight filters down to the surface that white ground shows almost no effect at all.

In between those two extremes, at 0.55 μm , at 0.65 μm , and at 0.94 μm , bright ground does improve illumination, albeit modestly. Red light at 0.65 μm shows the greatest increase with 70% higher surface flux than the black case. Near-infrared 0.94 μm light shows a 47% increase. These increases are significant, but do not change the overall results even on the nightside.

Beyond the terminator, the ratios remain roughly constant, indicating that nighttime illumination on Titan primarily derives from atmospheric scattering and not from light bouncing between the atmosphere and surface.

Cassini imaging shows surface 0.94 μm albedos ranging from 0.25 in the sand seas (Lorenz et al. 2006; Le Gall et al. 2011; Rodriguez et al. 2014; Karkoschka et al. 2017) up to 0.90 in Hotei Regio (Barnes et al. 2005; Soderblom et al. 2009; MacKenzie & Barnes 2016; Karkoschka et al. 2017). Therefore, any surface brightness enhancements to twilight illumination should be rather

small—a few tens of percent at most—on dunes or in interdune zones within Dragonfly’s initial sand sea landing ellipse.

ORCID iDs

Jason W. Barnes  <https://orcid.org/0000-0002-7755-3530>

References

- Anderson, C. M., Samuelson, R. E., Achterberg, R. K., Barnes, J. W., & Flasar, F. M. 2014, *Icar*, **243**, 129
- Barnes, J. W., Brown, R. H., Soderblom, L., et al. 2007, *Icar*, **186**, 242
- Barnes, J. W., Brown, R. H., Turtle, E. P., et al. 2005, *Sci*, **310**, 92
- Barnes, J. W., Clark, R. N., Sotin, C., et al. 2013, *ApJ*, **777**, 161
- Barnes, J. W., Lemke, L., Foch, R., et al. 2012, *ExA*, **33**, 55
- Barnes, J. W., MacKenzie, S. M., Young, E. F., et al. 2018, *AJ*, **155**, 264
- Barnes, J. W., Soderblom, J. M., Brown, R. H., et al. 2009, *P&SS*, **57**, 1950
- Brown, R. H., Soderblom, L. A., Soderblom, J. M., et al. 2008, *Natur*, **454**, 607
- Coustonis, A., Matson, D., Hansen, C., Lunine, J., & Lebreton, J.-P. 2009, ESA-SRE(2008)4
- Dhingra, R. D., Barnes, J. W., Brown, R. H., et al. 2018, *NatGe*, in Review
- Doose, L. R., Karkoschka, E., Tomasko, M. G., & Anderson, C. M. 2016, *Icar*, **270**, 355
- Fortney, J. J. 2005, *MNRAS*, **364**, 649
- García Muñoz, A., Lavvas, P., & West, R. A. 2017, *NatAs*, **1**, 0114
- Grieger, B. 2005, *P&SS*, **53**, 577
- Grieger, B., Lemmon, M. T., Markiewicz, W. J., & Keller, H. U. 2003, *P&SS*, **51**, 147
- Griffith, C. A., Doose, L., Tomasko, M. G., Penteado, P. F., & See, C. 2012, *Icar*, **218**, 975
- Griffith, C. A., Penteado, P., Rannou, P., et al. 2006, *Sci*, **313**, 1620
- Hirtzig, M., Bézard, B., Lellouch, E., et al. 2013, *Icar*, **226**, 470
- Karkoschka, E., McEwen, A., & Perry, J. 2017, *LPSC*, **48**, 2518
- Karkoschka, E., & Tomasko, M. G. 2010, *Icar*, **205**, 674
- Le Gall, A., Janssen, M. A., Wye, L. C., et al. 2011, *Icar*, **213**, 608
- Le Mouélic, S., Cornet, T., Rodriguez, S., et al. 2012a, *P&SS*, **73**, 178
- Le Mouélic, S., Rannou, P., Rodriguez, S., et al. 2012b, *P&SS*, **60**, 86
- Lemmon, M. T., Smith, P. H., & Lorenz, R. D. 2002, *Icar*, **160**, 375
- Levine, J. S., Wright, H. S., Gasbarre, J. F., et al. 2005, NASA GSFC Vision Mission Study, <https://ntrs.nasa.gov/archive/nasa/casi.ntrs.nasa.gov/20050212185.pdf>
- Lorenz, R. 2002, *AdAnS*, **112**, 563
- Lorenz, R. D. 2008, *JBIS*, **61**, 2
- Lorenz, R. D., Leary, J. C., Lockwood, M. K., & Waite, J. H. 2008, in AIP Conf. Ser. 969, Space Technology and Applications International Forum-STAIIF 2008, ed. M. S. El-Genk (Melville, NY: AIP), **380**
- Lorenz, R. D., & Newman, C. E. 2015, *AdSpR*, **56**, 190
- Lorenz, R. D., Tokano, T., & Newman, C. E. 2012, *P&SS*, **60**, 72
- Lorenz, R. D., Wall, S., Radebaugh, J., et al. 2006, *Sci*, **312**, 724
- Lunine, J., Lorenz, R. D., Smith, M., et al. 2005, NASA JPL Vision Mission Study, https://www.lpi.usra.edu/opag/oct_05_meeting/jpl_titan.pdf
- MacKenzie, S. M., & Barnes, J. W. 2016, *ApJ*, **821**, 17
- Maltagliati, L., Bézard, B., Vinatier, S., et al. 2015a, *Icar*, **248**, 1
- Maltagliati, L., Rodriguez, S., Sotin, C., et al. 2015b, in European Planetary Science Congress EPSC2015, **10**, 687
- McKay, C. P., Pollack, J. B., & Courtin, R. 1989, *Icar*, **80**, 23
- Porco, C. C., Baker, E., Barbara, J., et al. 2005, *Natur*, **434**, 159
- Rannou, P., McKay, C. P., & Lorenz, R. D. 2003, *P&SS*, **51**, 963
- Reh, K., Manger, T., Matson, D., et al. 2007, Jet Propulsion Laboratory, Titan Prebiotic Explorer (TiPEX) Mission Study Final Report
- Reh, K., Manger, T., Matson, D., et al. 2009, TSSM Final Report on the NASA Contribution to a Joint Mission with ESA, NASA Task Order NMO710851
- Richardson, J., Lorenz, R. D., & McEwen, A. 2004, *Icar*, **170**, 113
- Rodriguez, S., Garcia, A., Lucas, A., et al. 2014, *Icar*, **230**, 168
- Rodriguez, S., Le Mouélic, S., Sotin, C., et al. the VIMS Science Team 2006, *P&SS*, **54**, 1510
- Roe, H. G., Brown, M. E., Schaller, E. L., Bouchez, A. H., & Trujillo, C. A. 2005, *Sci*, **310**, 477
- Sittler, E. C., Cooper, J. F., Mahaffey, P., et al. TOAM Team 2006, *BAAS*, **38**, 1300
- Smith, B. A., Soderblom, L., Beebe, R. F., et al. 1981, *Sci*, **212**, 163
- Soderblom, L. A., Brown, R. H., Soderblom, J. M., et al. 2009, *Icar*, **204**, 610
- Sotin, C., Hayes, A., Malaska, M., et al. 2017, *LPSC*, **48**, 2306
- Sotin, C., Lawrence, K. J., Marmuse, F., et al. 2016, AAS/DPS Meeting, **48**, 515.08
- Stofan, E. R., Lorenz, R. D., Lunine, J. I., et al. 2010, *LPICo*, **1538**, 5270
- Tomasko, M. G., Archinal, B., Becker, T., et al. 2005, *Natur*, **438**, 765
- Tomasko, M. G., Bézard, B., Doose, L., Engel, S., & Karkoschka, E. 2008a, *P&SS*, **56**, 624
- Tomasko, M. G., Doose, L., Engel, S., et al. 2008b, *P&SS*, **56**, 669
- Turtle, E. P., Barnes, J. W., Trainer, M. G., et al. 2018, *LPSC*, **49**, 1641
- Turtle, E. P., Del Genio, A. D., Barbara, J. M., et al. 2011, *GeoRL*, **38**, L03203
- Turtle, E. P., Perry, J. E., McEwen, A. S., et al. 2009, *GeoRL*, **36**, L2204
- Vixie, G., Barnes, J. W., Bow, J., et al. 2012, *P&SS*, **60**, 52
- Young, E. F., Rannou, P., McKay, C. P., Griffith, C. A., & Noll, K. 2002, *AJ*, **123**, 3473